



An automated multi-order phase correction routine for processing ultra-wideline NMR spectra

Michael J. Jaroszewicz^{a,*}, Adam R. Altenhof^{b,c}, Robert W. Schurko^{b,c,*}, Lucio Frydman^{a,c,*}

^a Department of Chemical and Biological Physics, Weizmann Institute, Rehovot 7610001, Israel

^b Department of Chemistry and Biochemistry, Florida State University, Tallahassee, FL 32306, USA

^c National High Magnetic Field Laboratory, 1800 East Paul Dirac Drive, Tallahassee, FL 32310, USA

ARTICLE INFO

Keywords:

Ultra-wideline NMR Spectroscopy
Wideband Uniform-Rate Smooth-Truncation, (WURST)
Broadband Adiabatic Inversion-Cross Polarization (BRAIN-CP)
Second-order phase corrections
Data processing

ABSTRACT

Efficient acquisition of wideline solid-state nuclear magnetic resonance (NMR) spectra with patterns affected by large inhomogeneous broadening is accomplished with the use of broadband pulse sequences. These specialized pulse sequences often use frequency-swept pulses, which feature time-dependent phase and amplitude modulations that in turn deliver broad and uniform excitation across large spectral bandwidths. However, the resulting NMR spectra are often affected by complex frequency-dependent phase dispersions, owing to the interplay between the frequency-swept excitations and anisotropic resonance frequencies. Such phase distortions necessitate the use of multi-order non-linear corrections in order to obtain absorptive, distortion-free patterns with uniform phasing. Performing such corrections is often challenging due to the complex interdependence of the linear and non-linear phase contributions, and how these may affect the NMR signal. Hence, processing of these data usually involves calculating the spectra in magnitude mode wherein the phase information is discarded. Herein, we present a fully automated phasing routine that is capable of processing and phase correcting such wideline NMR spectra. Its performance is corroborated *via* processing of NMR data acquired using both the WURST-CPMG (Wideband, Uniform-Rate, Smooth Truncation with Carr-Purcell Meiboom-Gill acquisition) and BRAIN-CP (Broadband Adiabatic Inversion Cross Polarization) pulse sequences for a variety of nuclei (*i.e.*, ¹¹⁹Sn, ¹⁹⁵Pt, ³⁵Cl, ⁸⁷Rb, and ¹⁴N). Based on both simulated and experimental NMR datasets, it is demonstrated that automatic phase corrections up to and including second order can be readily achieved without *a priori* information regarding the nature of the phase-distorted NMR datasets, and independently of the exact manner in which time-domain NMR data are collected and subsequently processed. In addition, it is shown that NMR spectra acquired at both single and multiple transmitter frequencies that are processed with this automated phasing routine have improved signal-to-noise properties than those processed with conventional magnitude calculations, along with powder patterns that better match those of ideal NMR spectra, even for datasets possessing low signal-to-noise ratios and/or affected by spectral artifacts.

1. Introduction

Ultra-wideline (UW) solid-state NMR spectroscopy [1–3] refers to a collection of acquisition methods that include specialized pulse sequences [4–13], post-processing procedures [14–20], spin hyperpolarization techniques [21–24], and sophisticated hardware accessories [25–28], which address the difficulties hindering the acquisition of high-quality NMR spectra with inhomogeneous patterns spanning hundreds of kHz to several MHz – both under magic-angle spinning (MAS) and static conditions. A particularly important aspect of UW NMR that has opened large swaths of the Periodic Table to routine NMR investigation

has been the development and application of specialized pulse sequences featuring frequency-swept (FS) pulses capable of exciting, refocusing, and transferring spin polarization over broad frequency bandwidths (*e.g.*, MHz wide), which far outperform conventional rectangular pulses in these respects. These developments have led to an augmentation of signal-to-noise ratios (SNR), enhancement in resolution of patterns corresponding to unique chemical sites, and overall improvement in spectral quality and pattern uniformity. Most popular among these swept RF experiments are those that use Wideband, Uniform-Rate, Smooth-Truncation (WURST) pulses [29–31], for purposes of excitation and refocusing in Carr-Purcell Meiboom-Gill (CPMG)

* Corresponding authors.

E-mail addresses: jaroszem@med.umich.edu (M.J. Jaroszewicz), rschurko@fsu.edu (R.W. Schurko), lucio.frydman@weizmann.ac.il (L. Frydman).

<https://doi.org/10.1016/j.jmr.2023.107528>

Received 11 April 2023; Received in revised form 25 July 2023; Accepted 26 July 2023

Available online 28 July 2023

1090-7807/© 2023 Published by Elsevier Inc.

type sequences (*i.e.*, WURST-CPMG) [6], and for broadband cross polarization (*i.e.*, BRoadband Adiabatic Inversion Cross Polarization or BRAIN-CP) [8]. Fourier transformation (FT) of datasets acquired with WURST pulses yield spectra imbued with complex frequency-dependent phases originating from the interplay between the linear FS WURST pulses and the inhomogeneously-broadened NMR resonances, as well as from the collection and processing of spin echoes [31–35]. In the case of the former, the fact that spin packets occupy crystallites having distinct orientations with respect to the external magnetic field means that they will resonate, become excited, and/or refocus to form echoes at different time points throughout the WURST pulse; ultimately, this leads to the accumulation of both linear and quadratic phases across the breadth of the powder pattern. These quadratic phase contributions to the transverse NMR signals arise from evolution that is proportional to the product between a given isochromat's free-evolution time, and its corresponding orientation-dependent resonance frequency. As the former parametrically depends linearly on frequency due to a reliance on the FS pulse, the result is a quadratic dependence on time of the NMR signal – or, equivalently, on frequency after FT of the time-domain signal. The magnitude of these second-order quadratic phase dispersions are therefore sizable, scaling commensurately with both the total time period of the WURST pulses and the total powder pattern breadth. WURST pulses also contribute to the accumulation of first-order, linear, frequency-dependent phase effects across the powder pattern. Furthermore, additional linear phase contributions to the transverse signal also stem from the formation and subsequent processing of spin echoes, which routinely have maximum signal intensities in their centers, visible in the acquisition windows constituting the echo trains.

It is possible to deal with frequency-dependent phase dispersions brought about by these FS pulses by concatenating calibrated WURST $\pi/2$ excitation and π refocusing pulses, as shown in the acquisition of liquid-state NMR spectra [36–41]. Additionally, some of the complexity contained within these frequency-dependent phase profiles can also be suppressed by carefully calibrated WURST spin echo pulse parameterization, which can ultimately refocus the contributions of the quadratic phase to the transverse NMR signal over the course of single-echo acquisitions, as well as multi-echo acquisitions (for odd-numbered echoes) [33]. In principle, the degree of first- and second-order phase effects can be estimated during offline processing by considering the time at which the spin echo forms and the duration of the frequency-swept pulse, respectively [35,42]. Nevertheless, manual multi-order phase adjustments in the form of zeroth-, first-, and second-order corrections are almost always required for obtaining absorptive powder patterns that are free of distortions, which is important not only for UW NMR applications, but for other applications as well (*e.g.*, low field *ex vivo* NMR and MRI) [43–45].

As mentioned, a magnitude calculation, which involves summing the squares of both the real and imaginary spectral components and then square-rooting the result, is able to deliver UW NMR spectra that tend to have the correct overall powder pattern shape. While this sidesteps the need for complicated multi-order phase corrections, there are instances where it is highly desirable to retain the phase information and retrieve absorptive UW NMR spectra by applying multi-order phase corrections. Such examples include the accurate measurement of discontinuities, improvements of SNR, and achieving phase-sensitive absorptive line shapes in multi-dimensional correlation experiments. Finding suitable combinations of zeroth-, first-, and second-order phase coefficients is a non-trivial undertaking.

In this contribution, we introduce and discuss a method by which absorptive UW NMR spectra acquired with the WCPMG (WURST plus Carr-Purcell Meiboom-Gill) and BRAIN-CP (BRoadband Adiabatic Inversion Cross Polarization) pulse sequences can be readily achieved with the use of automated multi-order phase corrections. This is accomplished with a gradient-ascent-like principle acting on an iterative and automatic phase correction algorithm, which functions independently of the user and does not require any *a priori* information regarding

the nature of the experiment or the structure of the NMR data that is to be phased. In principle, our proposed method is capable of delivering phase corrections up to arbitrary order; with the use of numerous simulated and experimental NMR spectra acquired for spin-1/2, integer-spin, and half-integer spin quadrupolar nuclei, we effectively demonstrate that proper phase corrections can be robustly achieved up to and including second order. A detailed discussion pertaining to the operation of the proposed phasing algorithm, along with the simulated and experimental examples that showcase the ease with which multi-order phase corrections can be achieved, are discussed and presented in the following sections.

2. Experimental

2.1. Samples and Solid-State NMR Spectroscopy

2.1.1. Samples

Tin(II) oxide, dibutyltin(IV) oxide, tetraammine platinum(II) dichloride monohydrate, glycine hydrochloride, and α -glycine were all purchased from Sigma Aldrich and used as received without further purification. The identities and purities of the samples were verified through comparisons with previously reported NMR spectra and powder X-ray diffraction patterns. [8,46–48] All samples were ground into fine powders and packed into either 5 mm or 3.2 mm outer-diameter glass tubes that were sealed with Teflon tape.

2.1.2. Solid-State NMR spectroscopy

^{119}Sn and ^{35}Cl NMR spectra were acquired using a Bruker Avance NEO console and a 14.1 T ($\nu_0(^1\text{H}) = 600$ MHz) Magnex/Bruker wide-bore magnet operating at resonance frequencies of $\nu_0(^{119}\text{Sn}) = 223.77$ MHz and $\nu_0(^{35}\text{Cl}) = 58.787$ MHz. These NMR spectra were acquired with a home-built 5 mm double resonance (HX) probe. ^{195}Pt NMR spectra ($\nu_0(^{195}\text{Pt}) = 128.484$ MHz) were acquired using a Varian VNMRs console interfaced with an Oxford 14.1 T wide-bore magnet. A home-built static 3.2 mm HX probe was used to acquire these NMR spectra. ^{14}N NMR spectra were acquired using a Varian InfinityPlus NMR console interfaced with an Oxford 9.4 T wide-bore magnet ($\nu_0(^1\text{H}) = 400$ MHz). A static wide-line 5 mm HX probe were used for acquiring all ^{14}N NMR spectra ($\nu_0(^{14}\text{N}) = 28.894$ MHz), equipped with a low gamma accessory for probe tuning and matching. All data were collected under static conditions (*i.e.*, no MAS), using WCPMG windowed acquisitions whereby fifty to two hundred spin echoes were recorded in the presence of high-power ($\nu_1 = 50\text{--}75$ kHz) ^1H proton decoupling. Pulse width calibrations were carried out on the respective solution- or solid-state reference for each nuclide. NMR spectra acquired at a single transmitter frequency are referenced with respect to the carrier frequency, whereas spectra acquired with the VOCS method are referenced with respect to the Larmor frequency. Additional experimental details are provided in the main text below and in the [supporting information](#).

2.2. Numerical simulations

Numerical simulations were performed using the SIMPSON software program [49] (version 4.2.1) and custom-written MATLAB-based routines involving numerical integration of the Bloch equations. NMR datasets were simulated with either the WURST single-echo or WCPMG pulse sequences (Fig. S1b), which implemented WURST-80 amplitude profiles composed of 1000 points and of 50 μs duration (Fig. S1a). Linear frequency sweeps were used in all simulations, which swept over symmetric offsets (*i.e.*, the instantaneous transmitter offset is on resonance with both the nuclear Larmor frequency and the RF carrier frequency at the center of all WURST pulses) covering frequency ranges $\Delta\nu = 500$ kHz, 1000 kHz, and 2000 kHz, depending on the overall breadth of the targeted NMR spectrum. RF field strengths were optimized for each simulation by finding the WURST-A (excitation) and WURST-B (refocusing) nutation frequencies (denoted as $\nu_{1,A}$ and $\nu_{1,B}$, respectively) that

resulted in the most uniform excitation of the powder pattern. In cases where the frequency sweep rate (*i.e.*, denoted by R , where $R = \Delta\nu/\tau_p$ and τ_p denotes the pulse width) is the same for both the WURST-A excitation and WURST-B refocusing pulses, then the same RF field strength was used for excitation and refocusing of spin polarization (*i.e.*, $\nu_{1,A} = \nu_{1,B}$; this condition is most frequently employed in the experiments reported herein. In cases where the WURST-B refocusing pulse sweep rate is twice as fast as the WURST-A excitation pulse sweep rate ($R_B = 2R_A$), [36–39] which was always achieved by using the same 50 μs pulse width and doubling the linear frequency-sweep range ($\Delta\nu_B = 2\Delta\nu_A$), the value of the RF field strength for the WURST-B refocusing pulse was optimized to be 1.25–2 \times larger than that used for the WURST-A excitation pulse. [35] 32 spin echoes were explicitly simulated for all T_2 echo trains acquired with WCPMG, with each spin echo forming exactly in the center of the windowed acquisition period lasting either $\tau_{SE} = 128 \mu\text{s}$ or $\tau_{SE} = 256 \mu\text{s}$, and comprised of either 128 or 256 points. By comparison, WURST single-echo simulations were carried out assuming $\tau_{SE} = 1024$ or $\tau_{SE} = 2048 \mu\text{s}$, and are comprised of either 1024 or 2048 points respectively. In all cases, the initial density matrix (or thermal equilibrium magnetization vector) proportional to the longitudinal spin polarization was assumed, and an average over the powder pattern was calculated with either 986, 4180, or 28,656 (α,β) crystallites sampled according to the ZCW [50–51] scheme. All simulations were carried out at a magnetic field strength of $B_0 = 9.4 \text{ T}$, unless stated otherwise. Additional simulation details are provided in the sections below.

2.3. Data processing

All datasets were processed in MATLAB using custom-written processing routines, which are available upon request. Time-domain single spin echoes and CPMG echo trains were loaded into MATLAB, whereby each echo was individually multiplied with 2–10 kHz of Gaussian line broadening centered at the point of maximal signal intensity and the resulting datasets were zero-filled once. For some datasets, the spin echoes were added together in the time domain producing a single echo before zero filling. A fast Fourier transform (FFT) was used to generate the frequency-domain spectra, which were then either subjected to a magnitude calculation or an automatic iterative multi-order phase correction. No additional information was provided to the automated phase correction routine other than the unphased NMR spectrum. All of the simulated and experimental NMR spectra were phased using identical initial starting ranges for the zeroth-, first-, and second-order phase variables. With each subsequent iteration, each of the three phase variables were defined over progressively smaller ranges, whereby the limits decreased linearly with the iteration counter. In all cases, 15 iterations were used to determine the optimal phase coefficients (*i.e.*, up to and including second order), which were then used to obtain absorptive UW NMR spectra. The processing time varied between 0.5 and 3 min per spectrum. Additional details pertaining to the phase correction routine and the parameters used therein are explained with greater detail in the following sections. UW NMR spectra acquired with the Variable Offset Cumulative Spectroscopy (VOCS) [16] method were assembled in the frequency domain using either skyline projections or co-addition of the frequency-domain spectra.

3. Results and discussion

3.1. Overview

In the paragraphs that follow, the motivation is first provided for the approach at the heart of this new automatic phasing routine, which leads to purely absorptive UW NMR spectra collected using FS pulses. Then, several simulated and experimental UW NMR datasets are processed and automatically phase corrected to demonstrate the efficacy of this new technique, in which comparisons are made to NMR spectra that are processed with standard methods employing magnitude

calculations. For each of these datasets, the appearance of both the NMR spectrum and its corresponding transverse signal phase is discussed after the individual application of the optimal first-, zeroth-, and second-order phase correction. Simulations focused on UW NMR spectroscopy of spin-1/2 (^{119}Sn), spin-1 (^{14}N), and half-integer quadrupolar spin (^{87}Rb) nuclides, which were simulated with the WURST single-echo and WCPMG pulse sequences under static conditions. The aforementioned nuclei were selected as initial test examples on the basis of their ubiquity in many UW NMR applications, and their responses were simulated with NMR interactions whose magnitudes are chosen in such a way to lead to the formation of powder patterns that have comparable spectral breadths as those frequently encountered in the literature at commonly used magnetic field strengths (*e.g.*, $B_0 = 9.4 \text{ T}$ to 14.1 T). Discussions are grouped into two sections depending on whether the data were acquired at a single or at multiple transmitter frequencies, which demonstrates the robustness of these automatic phasing corrections; an analysis of the routine's performance as a function of the SNR is presented in the **Supporting Information**. Finally, analogous discussions and demonstrations are provided for an array of experimental NMR datasets acquired with WCPMG and BRAIN-CP pulse sequences under static conditions for commonly encountered spin-1/2 (^{195}Pt and ^{119}Sn), integer spin (^{14}N), and half-integer spin (^{35}Cl) quadrupolar nuclei.

3.2. Automated iterative multi-order phase corrections: Design and operation

In echo-based experiments like the ones considered herein, phase correction involves maximizing the signal intensity of the absorptive component of a complex-valued NMR dataset, while simultaneously minimizing the signal intensity of the corresponding dispersive component; by convention, these represent the real and imaginary parts of the NMR spectrum, respectively. Based on this, the task of performing a phase correction can be formulated as an optimization problem, whereby the integrated signal intensities for each of the orthogonal spectral components are correlated objective functions with corresponding global maximum and minimum target values within a multi-dimensional *phase space*. Stated in these terms, incremental variations of the domain elements belonging to this multidimensional phase space, which represent each of the phase coefficients uniquely affecting the transverse NMR signal (*i.e.*, the zeroth-, first-, second-order, *etc.* coefficients, denoted as $\text{ph}0$, $\text{ph}1$, and $\text{ph}2$, respectively) necessarily lead to incremental and smooth changes in the corresponding objective function values. Obtaining a uniformly phased NMR spectrum whose real component is wholly absorptive (having either net positive or net negative intensity), is possible by assuming that *an iterative and order-by-order sequential variation of each of the phase coefficients, which are defined over discrete intervals, leads to the formation of local maxima and/or local minima of the objective function values*. These values will approach the global extrema provided that the discretized phase regions are redefined over progressively smaller ranges with each subsequent iteration for all of the relevant phase coefficients affecting the transverse NMR signal. The validity of this assumption is further examined and validated in the sections below.

Reaching the global extrema for the objective function values – *i.e.*, the integrated signal intensities for each of the orthogonally assumed spectral components – was achieved using the multi-step procedure in **Fig. S2**. This algorithmic flow chart involves: (1) Apodization of the time-domain WCPMG dataset (here assumed to arise from ^{119}Sn), which is then subjected to echo co-addition and Fourier transformation (**Fig. 1a**). (2) Initialization of an iteration counter to a value of 1, and initial selection of all the first-order phase values that potentially affect the transverse NMR signal (defined over a wide and densely sampled region). It is noted that a first-order phase correction is performed before the zeroth- and second-order correction, since linear frequency-dependent phase dispersions outweigh those originating from zeroth- and second-order contributions (*vide infra*). [35] The integrated signal

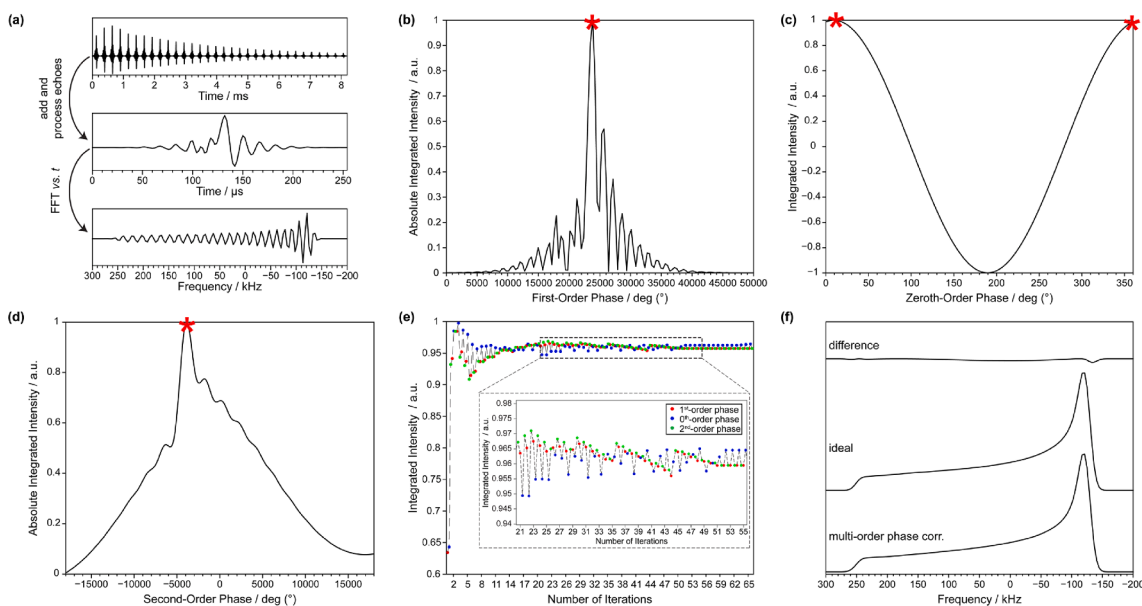


Fig. 1. The output generated at various stages throughout the automatic phasing routine using a (a) simulated ^{119}Sn dataset “acquired” with a WCPMG pulse sequence as an example. Thirty-two WCPMG spin echoes were simulated (a, top row), that were then individually processed, co-added in the time domain (a, middle row), and Fourier transformed (a, bottom row). (b) Absolute integrated signal intensity of the unphased powder pattern in (a) following a first-order phase correction (during the first iteration step) for 500 distinct phase values discretized from $\text{ph1} = 0^\circ$ to 50000° (both ph0 and $\text{ph2} = 0$ during this step). (c) Integrated intensity of the real part of the ^{119}Sn NMR spectrum as a function of 500 distinct zero-order phase values discretized from $\text{ph0} = 0^\circ$ to 360° ($\text{ph2} = 0$ and $\text{ph1} = 23820^\circ$). (d) Absolute integrated ^{119}Sn NMR spectral intensity as a function of 500 s-order phase corrections employing 500 distinct values discretized over a region covering $\text{ph2} = -18000^\circ$ to 18000° ($\text{ph1} = 23820^\circ$ and $\text{ph0} = 0^\circ$). (e) The largest integrated NMR spectral intensity values achieved after each successive ph1 (red dots), ph0 (blue dots), and ph2 (green dots) phase corrections as a function of the number of iterations. (f) Comparison between the ideal NMR spectrum and the multi-order phase corrected NMR spectrum plotted with their difference spectrum.

intensity of the real part of the powder pattern (Fig. 1a, bottom) is then calculated after first-order phase correction using each of the ph1 elements, with the values of ph0 and ph2 both having been initialized to 0 (Fig. 1b). Notice the point of maximum integrated intensity occurs at a first-order phase value of $\text{ph1} = 23820^\circ$ (points of maximum intensity are indicated by a red asterisk), which effectively matches the expected degree of first-order phase correction predicted by the *a priori* exactly known spin-echo delay, windowed acquisition time (denoted by τ_{SE}), and dwell time (denoted by dw): $\text{ph1} = 360 \cdot \tau_{\text{SE}} / (2 \cdot \text{dw}) = (360 \cdot 256 \mu\text{s}) / (2 \cdot 2 \mu\text{s}) = 23040^\circ$. [35] (3) Zero-order phase values are then defined and finely discretized over an interval covering $[0, 360^\circ]$. Using the ph1 value that was determined in the previous step, the integrated signal intensities are now calculated for each ph0 element using a zeroth-order + first-order phase correction, with the value of ph2 still equal to 0 (Fig. 1c). (4) Second-order phase values are then defined and discretized over a sufficiently wide and densely sampled region. Using the optimal ph0 and ph1 values, the integrated intensities are again calculated after a second-order and a simultaneous first- and zeroth-order phase correction for each of the ph2 elements (Fig. 1d). (5) The iteration counter is then incremented by 1, and steps (2)–(4) are repeated using the optimal ph2 , ph0 , and ph1 values in the ensuing phase corrections, and are redefined over progressively smaller limits, whose values inversely depend on the iteration counter. For instance, after the first iteration, the integrated intensities are calculated for a collection of ph1 values that are redefined over a range that has the optimal ph1 value occupying the middle element and whose overall excursion is smaller than that used in the previous iteration step. Likewise, the optimal values of ph2 and ph0 are used in subsequent first-order phase corrections (rather than 0, as was done in the first iteration), which leads to the formation of a powder pattern having a more positive net overall integrated intensity. Calculating and monitoring the integrated signal intensity for the real part of the NMR spectrum at each iteration step and using the phase values that result in its maximization within subsequent iterations allows for the accurate determination of ph1 , ph0 , and ph2

(Fig. 1e). Fig. 1e shows the maximum integrated signal intensity that results after each of the three sequential phase corrections (*i.e.*, first ph1 , then ph0 , then ph2 , which are represented by the red, blue, and green dots, respectively) over 66 iterations; clearly, a maximum value is approached with each subsequent iteration. The inset showcases the behaviour of the integrated signal intensity just before convergence is reached, at which point the value of the integrated intensity no longer significantly changes with subsequent iterations. At this point, the automatic phasing routine is exited and the three phase coefficients (ph0 , ph1 , and ph2) determined in the very last iteration are used to obtain an absorptively phased NMR spectrum, which for the ideal conditions assumed, is almost identical to the ideal NMR spectrum (Fig. 1f). Descriptions of the performance of this automatic multi-order phasing routine are presented below for a variety of simulated and experimental datasets, which showcase the behaviour of both the phase and spectral intensity after sequential phase correction with each of the optimal coefficients that are determined at the last iteration step.

3.3. Numerical simulations

3.3.1. Phase correcting UW NMR spectra simulated at a single transmitter frequency

3.3.1.1. CSA-Dominated patterns of spin-1/2 nuclei. Fig. 2 shows spin-1/2 NMR spectra of a single site affected by an axially symmetric chemical shift tensor, assumed to give rise to a powder pattern with a breadth of *ca.* 400 kHz dominated by the chemical shielding anisotropy (CSA). The datasets were simulated with the single-echo (top row) and CPMG (middle and bottom rows) pulse sequences employing ideal delta pulses for excitation and refocusing. The NMR spectra in the bottom row were processed by coadding the CPMG echo train into a single spin echo prior to FFT. For all figures presented herein, NMR spectra presented in red are processed with phase corrections whereas those presented in blue are processed with magnitude calculations (denoted as MC). Datasets

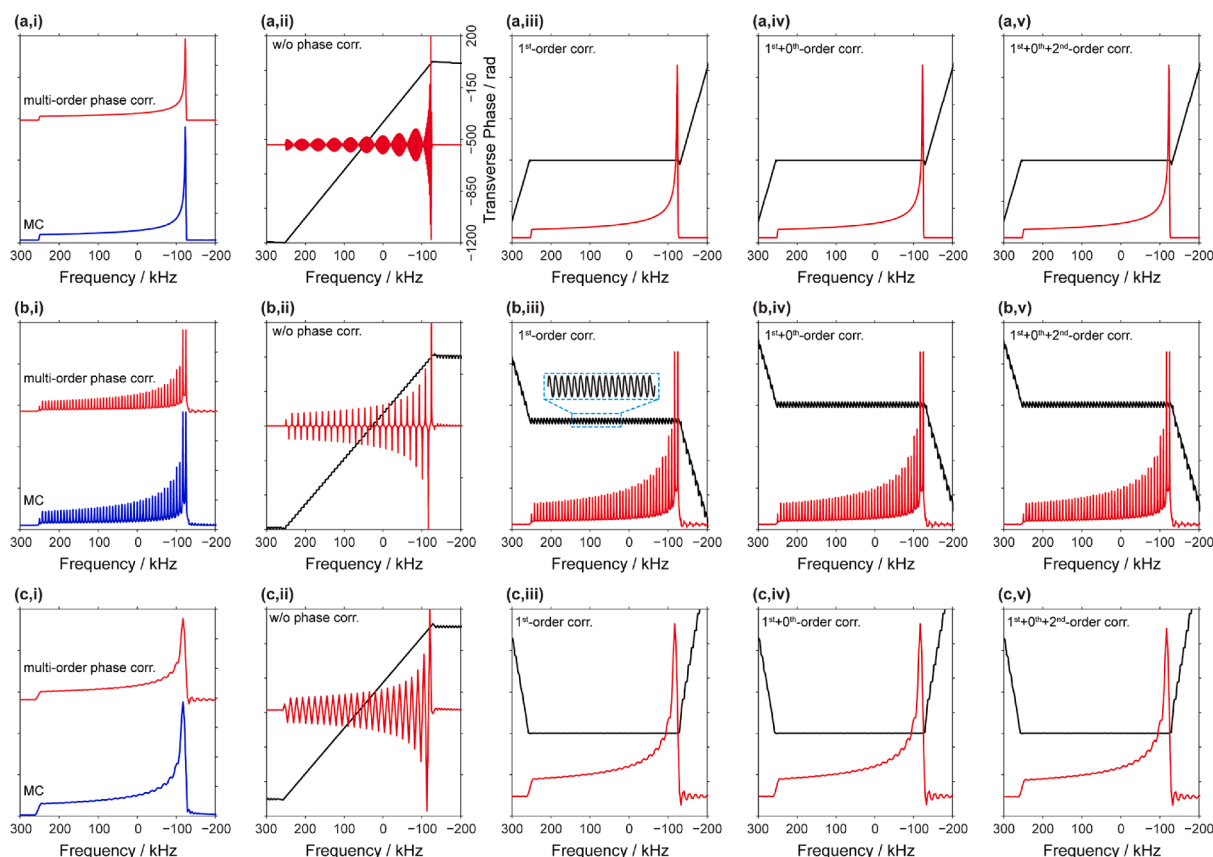


Fig. 2. Spin-1/2 NMR spectra simulated with the single echo (top row) and CPMG (middle and bottom rows) pulse sequences assuming ideal excitation and refocusing delta pulses for a single site with the following chemical shift tensor parameters (reported in the Haerberlen convention): $\delta_{\text{iso}} = 0$ kHz, $\delta = 250$ kHz, and $\eta = 0$. Datasets presented in red and blue were processed with phase corrections and magnitude calculation, respectively whereas datasets presented in black represent the transverse frequency-dependent phase across the breadth of the powder pattern. The datasets presented in the bottom row had their CPMG echo trains co-added in the time domain prior to Fourier transformation. Spin-1/2 NMR spectra in the left-most column ((a,i), (b,i), and (c,i)) show the phase corrected NMR spectra compared against their magnitude calculated (MC) counterparts. Each of the remaining columns showcase the resulting NMR datasets after various multi-order phase corrections, which are indicated in each plot (a total of 15 iterations were used in all cases, unless stated otherwise). Chemical shifts are reported with respect to the carrier frequency. Additional details pertaining to data simulation and processing are contained within Table S1 of the Supporting Information.

presented in black represent the frequency-dependent transverse NMR signal phase across the breadth of the powder pattern. The five columns showcase the NMR spectra and their corresponding frequency-dependent transverse phases after the application of various phase corrections, which employ the optimal phase coefficients. This structure of displaying data acquired with the use of different pulse sequences (*i.e.*, in different rows) and then phase corrected using different phase coefficients (*i.e.*, in different columns) is maintained throughout the rest of this work. In the leftmost column, the multi-order phase corrected NMR spectra, which were processed with the optimal values of ph0, ph1, and ph2, are plotted on the same scale as their magnitude calculated counterparts, both of which are virtually indistinguishable even though the former permits an accurate estimation of the SNR, retains the ability to differentiate positive and negative spin magnetization, and is useful for discriminating spurious artifact signals or interference. The datasets presented in the second left-most column show the NMR spectra and their corresponding phases that result immediately after FT without phase correction. We note the characteristic beat patterns of the NMR line shapes, which are indicative of large first-order phase dispersions resulting from the processing of time-domain spin echo and CPMG datasets, whose maximum signal intensities do not occur at the beginning of data acquisition. The reader is reminded that for all pulse sequences employed here, the RF pulses and delays are calibrated such that spin echoes form precisely in the middle of each windowed acquisition period. The presence of such large first-order phase dispersions is confirmed by the steep linear profiles of the frequency-dependent

transverse phase (black curves). We also note the varying degrees of phase dispersion present in each of the UW NMR patterns stems primarily from the different spin-echo times. Data presented in the middle were processed with the ideal amount of ph1 as determined from the automatic phasing routine, which produces absorptive NMR spectra with net positive intensity for all three acquisition and processing methods. In each case, the phase is uniform across the entire breadth of powder pattern, as indicated by the flat phase profiles over frequency regions that correspond to the NMR signal intensity. The blue inset in the center plot (Fig. 2b, iii) showcases the oscillatory phase imparted on the NMR powder pattern, which is the result of the multi-echoed CPMG acquisition and corresponds exactly to the individual spikelets in the pattern manifold. Importantly, as the automatic phasing routine is able to correctly identify that for these data, zeroth- and second-order corrections are not required for obtaining absorptive line shapes with uniform phases. This is demonstrated in the last two right columns, where even after 15 iterations through the automatic phasing routine, the optimal values of ph0 (second right-most column) and ph2 (right-most column) are both zero. This is consistent with the fact that these data were acquired with ideal monochromatic RF pulses having constant phase and amplitude, which do not impart second-order phase onto the transverse NMR signal and whose relative pulse phases were set such that ^{119}Sn spin polarization was excited along the $+x$ axis of the rotating frame, thereby avoiding the need for zeroth-order (*i.e.*, frequency-independent) phase corrections.

Fig. 3 shows NMR spectra of the same site as in Fig. 2, but simulated

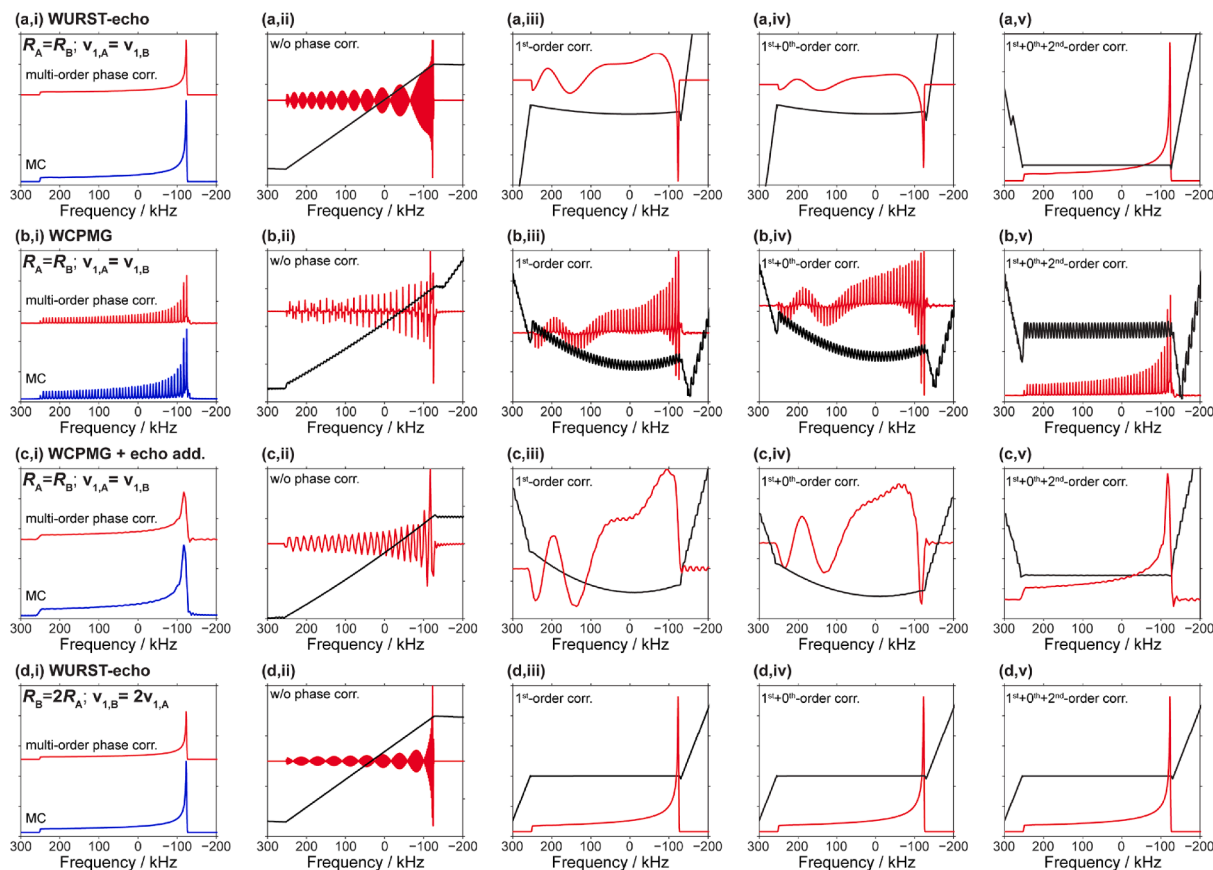


Fig. 3. Spin-1/2 NMR spectra simulated with the WURST echo (top and bottom row) and WCPMG (second and third rows from the top, in which the latter's echo train was co-added in the time domain prior to FT) pulse sequence for the same site as presented in Fig. 2. Datasets presented in the first, second, and third rows (as read from top to bottom) were simulated with 50 μ s WURST-A and WURST-B pulses each sweeping over a range of $\Delta\nu = 500$ kHz with RF field strengths of $\nu_{1,A} = \nu_{1,B} = 30$ kHz. The datasets in the bottom fourth row were simulated with WURST-B pulses sweeping over a range twice as large ($\Delta\nu = 1000$ kHz), which leads to a refocusing linear sweep rate that is twice as fast as the excitation linear sweep rate (i.e., $R_B = 2R_A$) and leads to the effective refocusing of second-order phase contributions across the entire breadth of the powder pattern. Chemical shifts are reported with respect the carrier frequency. Additional details pertaining to data simulation and processing are contained within Table S2 of the Supporting Information.

with WURST single-echo (top and bottom rows, (a) and (d)) and the WCPMG pulse sequences (middle two rows, (b) and (c), in which the WCPMG echoes in (c) were co-added together prior to Fourier transformation). Datasets presented in the top three rows ((a), (b), and (c)) were simulated with WURST-A and WURST-B pulses having the same linear sweep rates (i.e., $R_A = R_B$) and same RF field strengths ($\nu_{1,A} = \nu_{1,B}$), whereas the data in the bottom row were simulated with $R_B = 2R_A$ and $\nu_{1,B} = 2\nu_{1,A}$. As in Fig. 2, the spin-1/2 spectra processed with multi-order phase corrections employing the optimal ph0, ph1, and ph2 values are indistinguishable from those processed with magnitude calculations (left-most column). These NMR spectra are affected by multi-order phase distortions originating from combinations of frequency-independent and frequency dependent (linear and quadratic) contributions, where the magnitudes of the linear dispersions are significantly larger than those of zeroth- and second-order phase effects, as represented by the transverse phase profiles presented in the second column. Visually, it is not immediately obvious from these uncorrected spectral line shapes and corresponding phase profiles how many unique phase coefficients are affecting the transverse NMR signal; therefore, it is not apparent how many distinct phase corrections should be used to obtain absorptive NMR spectra having uniform phase. Nevertheless, the automatic phase correction is not affected by these difficulties, as higher-order successive phase corrections can be easily added to the algorithm and their resulting impact on the objective function values and convergence rate can be monitored. For these datasets however, phase corrections up to and including second order are sufficient for achieving

uniform phase across the entire powder pattern. The underlying smaller, but significant, quadratic contributions to the transverse NMR signal are revealed after the application of the optimal ph1 correction, as evidenced by the frequency-dependent second-order line shape distortions and the parabolic transverse phase profiles for datasets simulated with $R_A = R_B$ (middle column). The NMR spectrum in the last row (Fig. 3d,iii) was simulated with $R_B = 2R_A$, which in combination with the symmetric full echo acquisition and the simultaneous coherent refocusing of spin polarization for all isochromats, leads to the cancellation of all second-order phase contributions to the transverse NMR signal. This is evident in the formation of a uniformly phased absorptive NMR spectrum after ph1 correction. Considering now the top three rows, applying the optimal ph0 correction after the optimal ph1 correction (fourth column), does not alter the parabolic character of the transverse phase as expected, but serves to increase the overall net positive intensity. It is only after phase correction with the optimal ph2 correction that fully absorptive and distortion-free line shapes are achieved for the datasets collected with $R_A = R_B$ whose phase is uniform for all frequencies (right column). It is worth highlighting again that the automatic phase routine correctly identifies the order and number of distinct phase corrections that are needed to obtain uniform phase across the breadth of each pattern for both cases where $R_A = R_B$ and $R_B = 2R_A$.

3.3.1.2. Central-Transition powder patterns of half-integer quadrupolar nuclei. Fig. 4 shows CT solid-state NMR spectra of a spin-3/2 nucleus simulated for a single site characterized by an axially symmetric electric

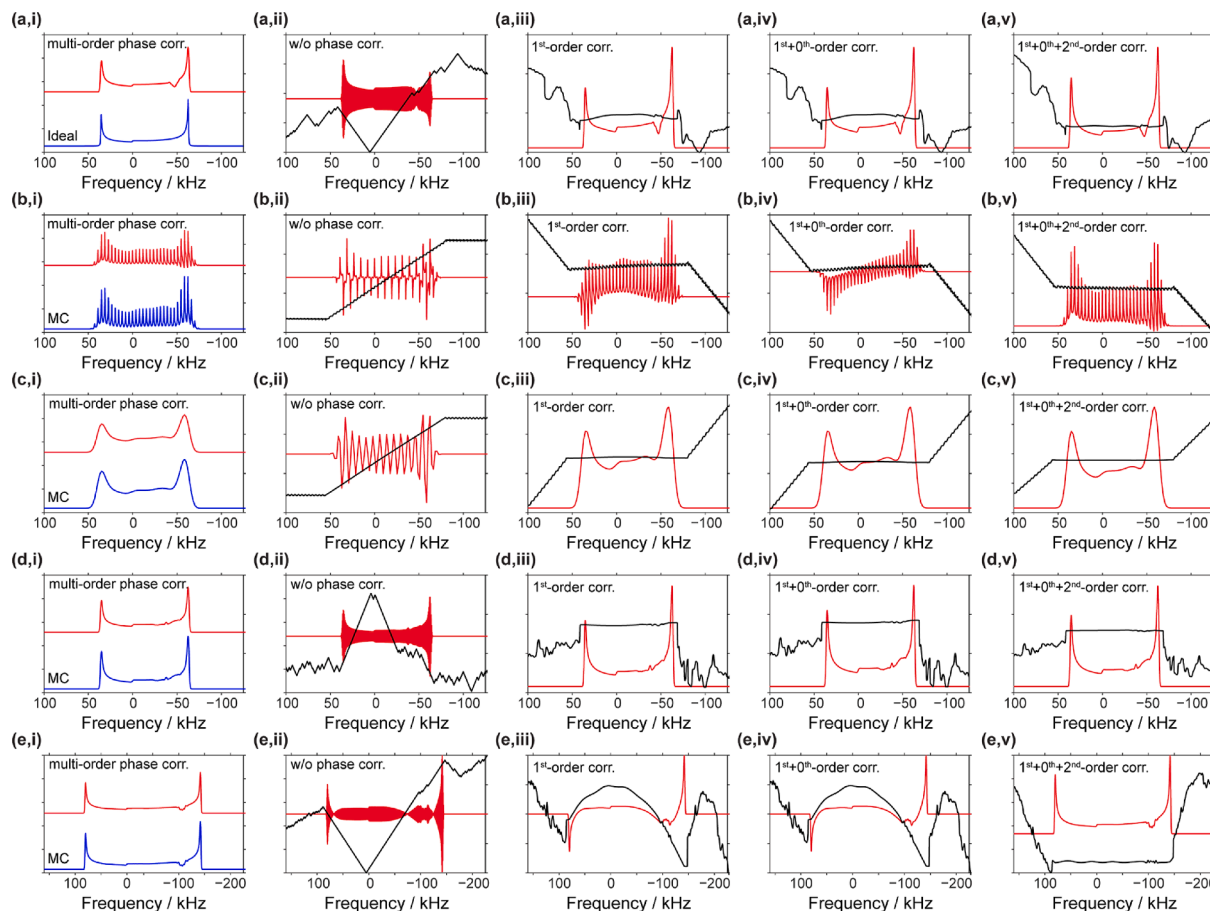


Fig. 4. Spin-3/2 central-transition NMR spectra simulated with the WURST echo (first, fourth, and fifth rows from the top) and WCPMG (second and third rows, with the latter echo train processed with echo co-addition prior to FFT) pulse sequences for 50 μ s WURST-A and WURST-B pulses sweeping 500 kHz (first, second, third, and fifth rows) and 2000 kHz (fourth row). NMR spectra in the top four rows and the last row were simulated with the following quadrupolar NMR parameters: $C_Q = 10$ MHz, $\eta_Q = 0$, $\delta_{iso} = 0$ kHz and $C_Q = 15$ MHz, $\eta_Q = 0$, $\delta_{iso} = 0$ kHz, respectively. Datasets in all but the fourth row were simulated with the same WURST pulse parameters ($\Delta\nu = 500$ kHz and $\nu_{1,A} = \nu_{1,B} = 18$ kHz), whereas a WURST-A and WURST-B linear sweep range of $\Delta\nu = 2000$ kHz was used in the simulation of the datasets in the fourth row. Additional details pertaining to data simulation and processing are contained within Table S3 of the Supporting Information.

field gradient (EFG) tensor ($\eta_Q = 0$), for two distinct quadrupolar coupling constants ($C_Q = 10.0$ MHz and 15.0 MHz for the top four rows and bottom row, respectively). As before, NMR spectra processed with multi-order phase corrections are virtually identical to both ideal NMR spectra and those processed with magnitude calculations (first column) for datasets acquired with both a single spin echo (rows (a), (d), and (e)), WCPMG (row (b)), and WCPMG echo train co-addition (row (c)). It is worth mentioning at this point that each of these NMR datasets are affected by the same spectral distortion located at *ca.* -45 kHz, which corresponds to the orientation-dependent resonance frequency of isochromats having orientations at or near the magic angle.¹³ At these orientations, satellite and central transitions are effectively overlapping, leading to efficient population transfer from the latter to the former and a subsequent loss of spectral intensity. Nevertheless, this sequence-related feature does not affect the performance of the automatic phase routine. For all NMR spectra, the linear frequency-dependent contributions to the transverse phase dominate (second column), just as observed for their spin-1/2 counterparts. Unlike the spin-1/2 examples, however, the contributions of the second-order phase effects are significantly smaller in the NMR spectra for the site affected by the smaller of the two quadrupolar couplings (top four rows, $C_Q = 10.0$ MHz). This results from targeting a relatively narrower *ca.* 125 kHz powder pattern, in comparison to both the wider *ca.* 250 kHz powder pattern in the bottom row ($C_Q = 15.0$ MHz), as well as the *ca.* 400 kHz-wide CSA-dominated patterns presented in Fig. 2 (*vide infra*). The second-order phase contributions are not readily apparent in the NMR spectra (nor in the transverse

phase profiles) for datasets simulated or processed with a single spin echo for the top four rows, with only the WCPMG spikelet manifold (Fig. 4b,ii) exhibiting a discernible second-order phase distortion. The datasets presented in the bottom two rows demonstrate the relative contributions of the two factors that contribute to the magnitude of second-order phase dispersions – namely the total frequency-sweep range of the RF and the total breadth of the targeted NMR spectrum. The data shown in row (d) were simulated with the exact same conditions as the top three rows, but with a sweep range for the WURST pulses covering 2 MHz, rather than 500 kHz as was done in the top three rows. As can be seen from the transverse phase profile across the breadth of the powder pattern (Fig. 4d,iii), the larger WURST sweep range does not increase the magnitude of the second-order phase dispersion. Conversely, exciting a powder pattern of two times the breadth with WURST pulses sweeping 500 kHz (the same sweep range as the top three rows) leads to a significant increase of the second-order phase across the breadth of the pattern (Fig. 4e,iii). This stems from the fact that the maximum degree of second-order frequency-dependent phase is proportional to both the post-excitation evolution time of a given isochromat and its orientation-dependent resonance frequency. [33–34] For the narrower powder pattern an overall smaller range of orientation-dependent resonance frequencies are non-zero, in comparison to the larger pattern, which results in a smaller accumulation of second-order phase. A discussion pertaining to the automatic phasing routine’s performance as a function of the SNR is provided in Fig. S4, which shows that correct phase corrections can be performed for SNRs as low as 10.

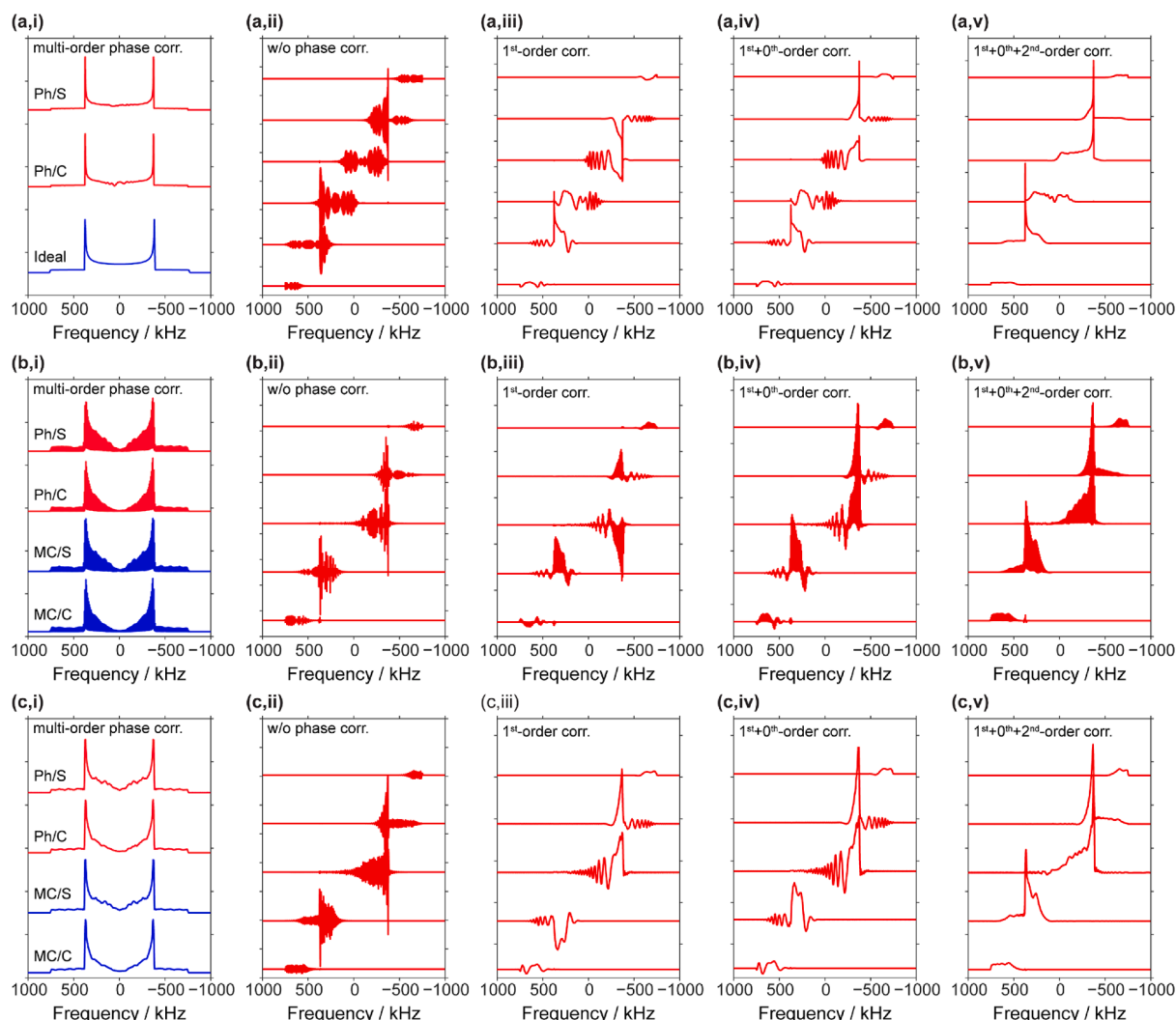


Fig. 5. Simulated frequency-stepped ^{14}N -like NMR datasets acquired with the WURST echo (top row) and WCPMG (middle and bottom rows, in which the latter's echo train was echo co-added prior to FFT) pulse sequences for a single spin-1 environment influenced solely by the first-order quadrupolar interaction with $C_Q = 1.0$ MHz, $\eta_Q = 0$, and $\delta_{\text{iso}} = 0$ kHz. The use of WURST pulses having intentionally narrow (*i.e.*, narrow in comparison to the total pattern breadth) linear sweep ranges of $\Delta\nu = 500$ kHz necessitates the use of frequency-stepped VOCS acquisition, in which the transmitter frequency was stepped in 100 kHz increments across the *ca.* 2 MHz pattern from -1000 kHz to 1000 kHz (only a few sub-spectra are shown for clarity). In each case, a total of twenty-one sub-spectra were simulated with each sub-spectrum subjected to automatic phase correction. The NMR spectra simulated with frequency stepping presented in the left most column were assembled in the frequency domain using both skyline projections (denoted with S) and co-addition (denoted with C). The corresponding phase profiles are omitted here for the sake of clarity, but Fig. S2 shows the phase information overlaid with the NMR spectra presented in the top row. Chemical shifts are referenced with respect to $\nu_0(^{14}\text{N}) = 28.905$ MHz. Additional details pertaining to data simulation and processing are contained within Table S4 of the Supporting Information.

3.3.2. Phase correcting UW NMR spectra acquired with frequency-stepped acquisitions

Many NMR-insensitive nuclei are affected by very large anisotropic NMR interactions which result in the formation of powder patterns whose breadths far exceed the excitation and/or detection bandwidths of the transmitting electronics and rf probe circuitry. As a result, these UW NMR spectra must be mapped out by first collecting multiple sub-spectra at distinct transmitter frequencies across the breadth of the entire pattern, which are then assembled offline using skyline projections or simple frequency-domain co-addition; such frequency-stepped acquisitions are known as Variable Offset Cumulative Spectroscopy (VOCS). The VOCS methodology is routinely employed, for example, in the collection of ^{14}N NMR spectra, whose powder pattern breadths often exceed 1 MHz [52–54]. NMR spectra representative of such spin-1 scenarios ($C_Q = 1.0$ MHz and $\eta_Q = 0$) are shown in Fig. 5, for powder patterns often encountered when targeting pseudo-tetrahedral sp^3 -hybridized ammonium sites prevalent in amino acids. These NMR simulations also serve to demonstrate that the same uniform phase can

be achieved across the entire breadth of the projected powder pattern regardless of the location of the transmitter frequency in an VOCS acquisition routine. These spin-1 NMR spectra were simulated with the WURST single-echo (top row) and WCPMG (middle and bottom rows with the latter having been processed with echo co-addition prior to FT) pulse sequences employing WURST pulses that deliberately swept over narrow (*i.e.*, 500 kHz) regions – in comparison to the total pattern breadth – in order to emulate limited detection bandwidth. Only a few individual sub-spectra (six for the top row and five for the bottom two rows) are shown without their corresponding transverse phase profiles (Fig. S3 shows the transverse phase for the dataset in the top row) for the sake of clarity and readability; a total of 21 sub-spectra covering a 2 MHz range centered about the Larmor frequency were simulated in each case and then subjected to automatic phase corrections. Excellent correspondence is observed between the phase-corrected NMR spectra, their corresponding MC counterparts, and the ideal spin-1 spectrum (Fig. 5a, i), irrespective of whether the overall pattern is assembled with a skyline projection or frequency-domain co-addition (denoted by the letters S

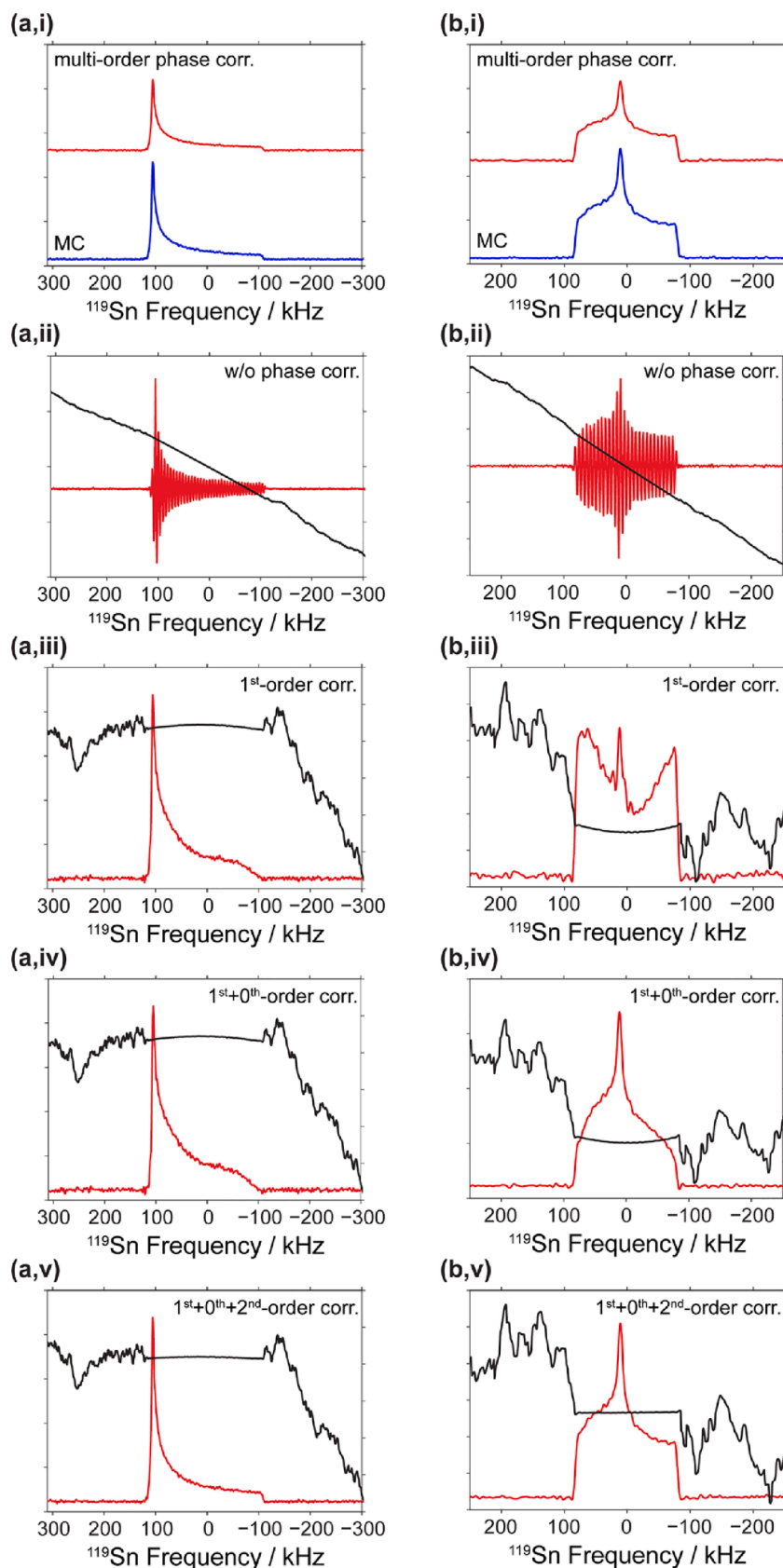


Fig. 6. Experimental ^{119}Sn spectra collected at $B_0 = 14.1$ T using the (a) WCPMG and (b) BRAIN-CP pulse sequences for samples of SnO (SNR = 280) and DBTO (SNR = 230), respectively. Chemical shifts are referenced with respect to the carrier frequency in each case. Additional details pertaining to the acquisition and processing methods are contained within Tables S5-S6 of the [Supporting Information](#).

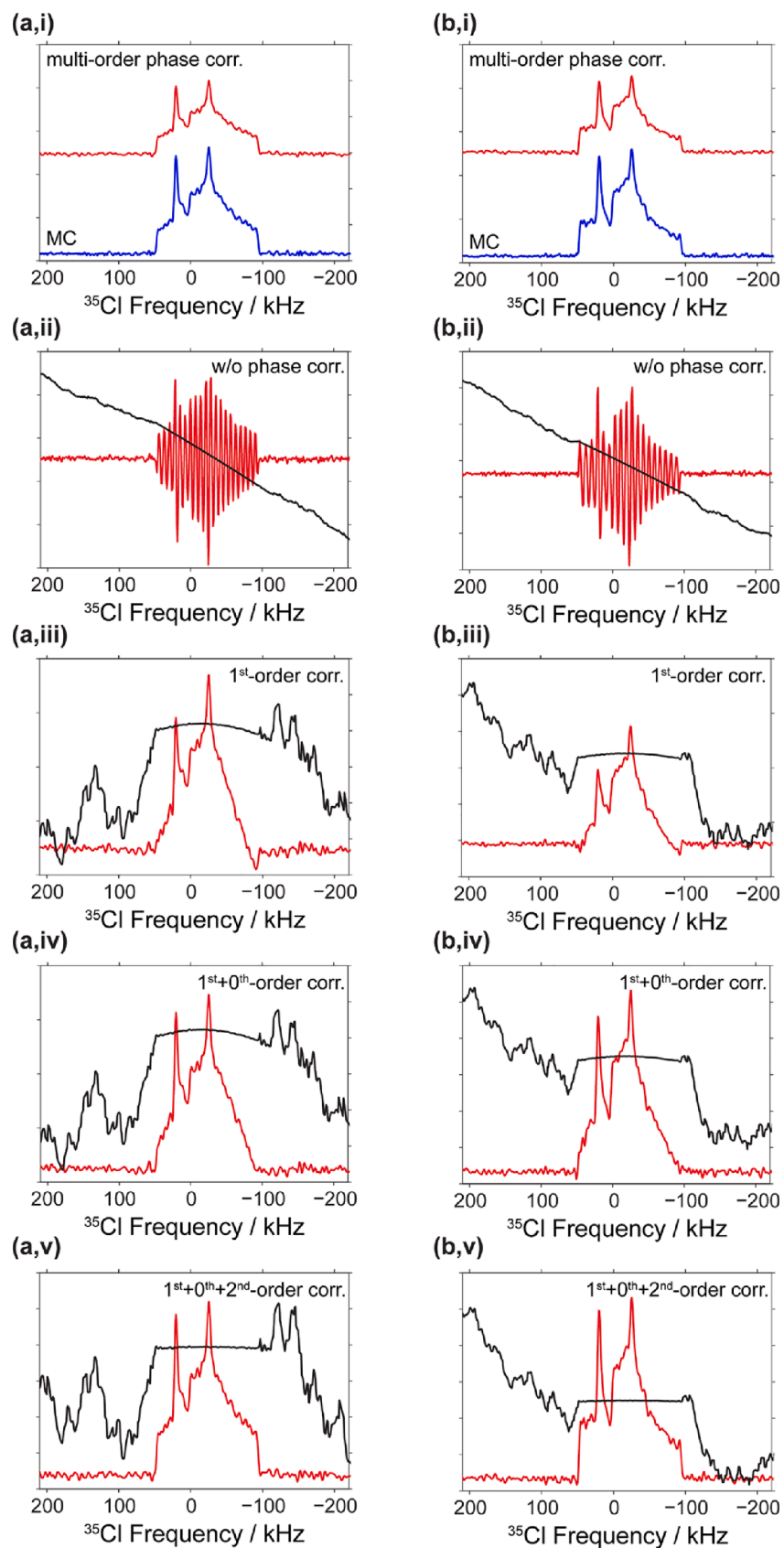


Fig. 7. Experimental ^{35}Cl spectra collected at $B_0 = 14.1$ T using the (a) WCPMG (SNR = 80) and (b) BRAIN-CP (SNR = 100) pulse sequences for a sample of glycine HCl. Chemical shifts are referenced with respect to the carrier frequency in each case. Additional details pertaining to the acquisition and processing methods are contained within [Table S7](#) of the [Supporting Information](#).

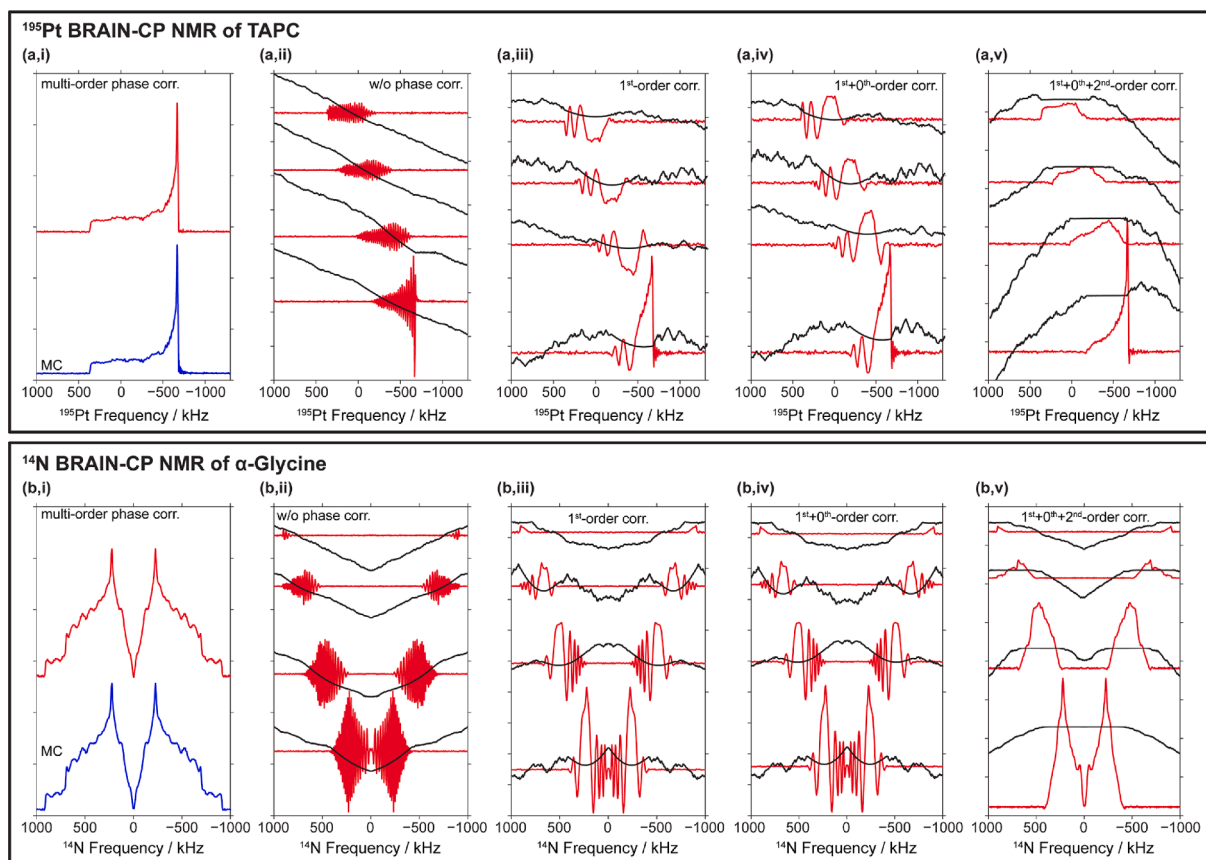


Fig. 8. Experimental ^{195}Pt (top) and ^{14}N NMR spectra (bottom) collected at $B_0 = 14.1$ T and 9.4 T, respectively using the BRAIN-CP pulse sequence. ^{195}Pt and ^{14}N NMR spectra were collected for tetraamine platinum (II) chloride monohydrate (TAPC) and α -glycine, respectively (SNR = 230 and 210, respectively). The ^{195}Pt NMR spectrum was reconstructed from four individual sub-spectra, whereas a total of eleven sub-spectra (only eight are shown for clarity) were acquired for the ^{14}N NMR spectrum with both spectra assembled in the frequency domain using skyline projections. The total ^{14}N pattern was assembled with spectral mirroring, which involved reflecting the low frequency side of the ^{14}N spectrum about $\nu_0(^{14}\text{N})$. Chemical shifts are referenced with respect to $\nu_0(^{195}\text{Pt}) = 128.95$ MHz and $\nu_0(^{14}\text{N}) = 28.89$ MHz. Additional details pertaining to the acquisition and processing methods are contained within Tables S8-S9 of the [Supporting Information](#).

and C in the figure labels, respectively). The Fourier-transformed NMR spectra (second column) show the characteristic phase distortions typical of large first-order phase contributions (see [Fig. S3](#)). After phase correction with the optimal value of ph1 (middle column), the underlying second-order contributions become distinguishable, which exhibit a much larger second-order phase effect than any of the previously discussed examples, resulting from the larger (ca. 500 kHz/sub-spectrum) breadth of orientation-dependent resonance frequencies. After subsequent zeroth- and second-order phase corrections applying the optimal values of ph0 and ph2 , each sub spectrum becomes absorptively phased, and can be assembled to yield the full spin-1 pattern (left column). It is noted that the algorithm determined the same phase values for each sub-spectrum.

3.4. Experimental validations

3.4.1. Phase correcting UW NMR spectra acquired at a single transmitter frequency

[Fig. 6](#) and [Fig. 7](#) each show two experimental ^{119}Sn and ^{35}Cl NMR datasets, respectively collected for three different compounds – tin (II) oxide (SnO , [Fig. 6a](#)), dibutyltin oxide (DBTO, [Fig. 6b](#)), and glycine hydrochloride (glycine HCl, [Fig. 7](#)) – using the WCPMG and BRAIN-CP pulse sequences. Examination of the four datasets in the top row reveals that the automatic phasing routine phase corrects all NMR spectra, which are absorptively-phased powder patterns that are virtually identical to their ideal counterparts on the basis of overall pattern intensity, shape, and uniformity. First-order linear phase dispersions dominate the

transverse NMR signal in all uncorrected datasets (second row). Second-order frequency-dependent phase effects are smaller by comparison (third and fourth rows), as evidenced by the smaller parabolic excursions of the transverse phase (black curves) and the fact that the line shapes obtained after zeroth-order correction (fourth row) closely match those presented in the first row, having only minor distortions localized at the periphery of each of the powder patterns. These spectral distortions, though minor, would ultimately hinder an accurate fitting and subsequent retrieval of the NMR tensor parameters; a second-order phase correction eliminates these distortions, since a completely uniform phase is achieved across the breadth of each NMR pattern (fourth column).

3.5. Phase correcting UW NMR spectra acquired with frequency-stepped acquisition

Frequency-stepped BRAIN-CP ^{195}Pt and ^{14}N UW NMR spectra of tetraamine platinum (II) chloride monohydrate (TAPC) and α -glycine are shown in the top and bottom rows, respectively, of [Fig. 8](#). A total of four and eleven sub-spectra were collected for ^{195}Pt and ^{14}N (only eight are shown for clarity), respectively, each of which was individually subjected to the automatic phasing routine and then skyline projected in the frequency domain to reconstruct the total powder pattern; similar VOCS spectra were obtained whether an MC or multi-order phase correction are used for data processing (left-most column). It is important to note that the automatic phasing routine is compatible with existing UW NMR processing methods such as spectral mirroring, which

is also used for acquiring ^{14}N UW NMR spectra of systems where the first-order quadrupolar interaction dominates all other NMR interactions. Both the top and bottom datasets show large first-order and second-order phase dispersions (second left-most and middle columns, respectively), the latter of which originates from the much larger inhomogeneously-broadened line width of each NMR spectrum. Applying the optimal second-order phase correction generates absorptive line shapes for both ^{195}Pt and ^{14}N , with both having uniform phase for all individual sub spectra irrespective of the transmitter frequency (right-most column).

4. Conclusions

UW NMR spectra of spin-1/2 (^{119}Sn and ^{195}Pt), spin-1 (^{14}N), and spin-3/2 (^{35}Cl and ^{87}Rb) nuclei affected by large anisotropic NMR interactions can be processed with automatic multi-order phase corrections to give absorptive, uniform powder patterns. Designing such a processing routine is possible by formalizing the task of a multi-order phase correction as an optimization problem, in which the integrated area of both the absorptive and dispersive spectral components are treated as correlated objective functions that depend, in a multi-parametric fashion, on each of the individual phase coefficients affecting the transverse NMR signal. Discretizing these phase coefficients over broad phase ranges and then monitoring how the objective function values change over the course of successive phase corrections implemented for each of these elements – applied in an order-by-order sequential manner – allows for the identification of local extrema. Identifying the phase values that give the global maximum and minimum for the absorptive and dispersive objective functions, respectively, is possible by repeating the order-by-order sequential phase corrections over progressively smaller phase ranges until the objective function values no longer significantly change with subsequent iterations. The resulting automatic phasing routine does not require any information pertaining to the nature of the NMR data that is to be phased and remains insensitive to the exact structure of the time-domain FID (*i. e.*, datasets collected with CPMG composed of multiple spin echoes or processed with echo co-addition can be equally phase corrected). Phased spectra can be readily obtained for datasets affected by spectral artifacts and characterized by low SNR; in fact, NMR spectra with SNR as low as 10 can be readily and accurately phase corrected. Simulated and experimental NMR datasets that were acquired with the WCPMG and BRAIN-CP pulse sequences on different spectrometers operating at different magnetic field strengths employing both home-built and commercial hardware were all readily processed with this new phase correction routine, which further demonstrates its robustness. Moreover, this method should be applicable for processing any NMR spectrum provided the SNR is large enough. The processing routine may fail at arriving at a phased NMR spectrum in cases where the SNR is not sufficient and the standard deviation of the noise is comparable in magnitude to the real signal intensity.

Declaration of Competing Interest

The authors declare that they have no known competing financial interests or personal relationships that could have appeared to influence the work reported in this paper.

Data availability

Data will be made available on request.

Acknowledgments

R.W.S. and A.R.A. would like to thank the National Science Foundation Chemical Measurement and Imaging Program, with partial co-funding from the Solid State and Materials Chemistry Program (NSF-

2003854), for supporting this work, as well as The Florida State University and the National High Magnetic Field Laboratory (NHMFL), which is funded by the National Science Foundation Cooperative Agreement (DMR-1644779 and DMR-2128556) and by the State of Florida. M.J.J. would like to thank the Perlman Family Foundation for a student-initiated research grant and the EU Horizon 2020 program (Marie Skłodowska-Curie Grant 642773). Also, M.J.J. acknowledges and thanks Dr. Mihajlo Novakovic for designing the TOC graphic. L.F. thanks the Minerva Foundation (Germany), the Israel Science Foundation (grants 3594/21 and 1874/22) and the Perlman Family Foundation; he holds the Bertha and Isadore Gudelsky Professorial Chair and Heads the Clore Institute for High-Field Magnetic Resonance Imaging and Spectroscopy at the Weizmann Institute, whose support is also acknowledged.

Appendix A. Supplementary material

Supplementary data to this article can be found online at <https://doi.org/10.1016/j.jmr.2023.107528>.

References

- [1] R.W. Schurko, Acquisition of Wideline Solid-State NMR Spectra of Quadrupolar Nuclei, in: R.E. Wasylshen, S.E. Ashbrook, S. Wimperis (Eds.), *Encyclopedia of Magnetic Resonance*, John Wiley & Sons Ltd, Chichester, 2012.
- [2] R.W. Schurko, Ultra-Wideline solid-state NMR spectroscopy, *Acc. Chem. Res.* 46 (2013) 1985–1995.
- [3] L.A. O'Dell, Ultra-Wideline Solid-State NMR: Developments and Applications of the WCPMG Experiment, in: G. Webb (Ed.), *Modern Magnetic Resonance*, Springer, Cham, 2017, pp. 1–22.
- [4] L.A. O'Dell, R.W. Schurko, QCPMG using adiabatic pulses for faster acquisition of ultra-wideline NMR spectra, *Chem. Phys. Lett.* 464 (2008) 97–102.
- [5] K.K. Dey, J.T. Ash, N.M. Trease, P.J. Grandinetti, Trading sensitivity for information: Carr-Purcell-Meiboom-Gill acquisition in solid-state NMR, *J. Chem. Phys.* 133 (2010) 1–10.
- [6] A.W. MacGregor, L.A. O'Dell, R.W. Schurko, New methods for the acquisition of ultra-wideline solid-state NMR spectra of Spin-1/2 nuclides, *J. Magn. Reson.* 208 (2011) 103–113.
- [7] A.J. Pell, G. Kervern, L. Emsley, M. Deschamps, D. Massiot, P.J. Grandinetti, G. Pintacuda, Broadband inversion for MAS NMR with single-sideband-selective adiabatic pulses, *J. Chem. Phys.* 134 (2011) 24113–24117.
- [8] K.J. Harris, A. Lupulescu, B.E.G. Lucier, L. Frydman, R.W. Schurko, Broadband adiabatic inversion pulses for cross polarization in wideline solid-state NMR spectroscopy, *J. Magn. Reson.* 224 (2012) 38–47.
- [9] K. Basse, S.K. Jain, O. Bakharev, N.C. Nielsen, Efficient polarization transfer between spin-1/2 and ^{14}N nuclei in solid-state MAS NMR spectroscopy, *J. Magn. Reson.* 244 (2014) 85–89.
- [10] M. Shen, J. Trébosc, O. Lafon, Z. Gan, F. Pourpoint, B. Hu, Q. Chen, J.P. Amoureux, Solid-State NMR indirect detection of nuclei experiencing large anisotropic interactions using spinning sideband-selective pulses, *Solid State Nucl. Magn. Reson.* 72 (2015) 104–117.
- [11] A.J. Rossini, M.P. Hanrahan, M. Thuo, Rapid acquisition of wideline MAS solid-state NMR spectra with fast MAS, proton detection, and dipolar HMQC pulse sequences, *Phys. Chem. Chem. Phys.* 18 (2016) 25284–25295.
- [12] M. Pruski, Indirect detection of infinite-speed MAS solid-state NMR spectra, *J. Magn. Reson.* 276 (2017) 95–102.
- [13] A.R. Altenhof, A.W. Lindquist, L.D.D. Foster, S.T. Holmes, R.W. Schurko, On the use of frequency-swept pulses and pulses designed with optimal control theory for the acquisition of ultra-wideline NMR spectra, *J. Magn. Reson.* 309 (2019), 106612.
- [14] T.J. Bastow, M.E. Smith, ^{91}Zr NMR characterisation of phases in transformation toughened zirconia, *Solid State Nucl. Magn. Reson.* 1 (1992) 165–174.
- [15] D. Massiot, I. Farnan, N. Gautier, D. Trumeau, A. Trokner, J.P. Coutures, ^{71}Ga and ^{69}Ga nuclear magnetic resonance study of beta- Ga_2O_3 : Resolution of four- and six-fold coordinated Ga sites in static conditions, *Solid State Nucl. Magn. Reson.* 4 (1995) 241–248.
- [16] A. Medek, V. Frydman, L. Frydman, Central transition nuclear magnetic resonance in the presence of large quadrupole couplings: cobalt-59 nuclear magnetic resonance of cobaltophthalocyanines, *J. Phys. Chem. A* 103 (1999) 4830–4835.
- [17] A. Lupulescu, M. Kotecha, L. Frydman, Relaxation-Assisted separation of chemical sites in NMR spectroscopy of static solids, *J. Am. Chem. Soc.* 125 (2003) 3376–3383.
- [18] L.A. O'Dell, A.J. Rossini, R.W. Schurko, Acquisition of ultra-wideline NMR spectra from quadrupolar nuclei by frequency stepped WURST-QCPMG, *Chem. Phys. Lett.* 468 (2009) 330–335.
- [19] A.J. Pell, R.J. Clément, C.P. Grey, L. Emsley, G. Pintacuda, Frequency-Stepped acquisition in nuclear magnetic resonance spectroscopy under magic angle spinning, *J. Chem. Phys.* 138 (2013), 114201.

- [20] M.J. Jaroszewicz, L. Frydman, R.W. Schurko, Relaxation-Assisted separation of overlapping patterns in ultra-wideline NMR spectra, *J. Phys. Chem. A* 121 (2017) 51–65.
- [21] A.J. Rossini, L. Emsley, L.A. O'Dell, Dynamic nuclear polarisation enhanced 14N overtone MAS NMR spectroscopy, *Phys. Chem. Chem. Phys.* 16 (2014) 12890–12899.
- [22] T. Kobayashi, F.A. Perras, T.W. Goh, T.L. Metz, W. Huang, M. Pruski, DNP-enhanced ultrawideline solid-state NMR spectroscopy: studies of platinum in metal-organic frameworks, *J. Phys. Chem. Lett.* 7 (2016) 2322–2327.
- [23] D.A. Hirsh, A.J. Rossini, L. Emsley, R.W. Schurko, 35Cl dynamic nuclear polarization solid-state NMR of active pharmaceutical ingredients, *Phys. Chem. Chem. Phys.* 18 (2016) 25893–25904.
- [24] T. Kobayashi, F.A. Perras, A. Murphy, Y. Yao, J. Catalano, S.A. Centeno, C. Dybowski, N. Zumbulyadis, M. Pruski, DNP-Enhanced ultrawideline 207Pb solid-state NMR spectroscopy: an application to cultural heritage science, *Dalt. Trans.* 46 (2017) 3535–3540.
- [25] K. Yamauchi, J.W.G. Janssen, A.P.M. Kentgens, Implementing solenoid microcoils for wide-line solid-state NMR, *J. Magn. Reson.* 167 (2004) 87–96.
- [26] J.A. Tang, L.A. O'Dell, P.M. Aguiar, B.E.G. Lucier, D. Sakellariou, R.W. Schurko, Application of static microcoils and WURST pulses for solid-state ultra-wideline NMR spectroscopy of quadrupolar nuclei, *Chem. Phys. Lett.* 466 (2008) 227–234.
- [27] O. Pecher, D.M. Halat, J. Lee, Z. Liu, K.J. Griffith, M. Braun, C.P. Grey, Enhanced efficiency of solid-state NMR investigations of energy materials using an External Automatic Tuning/Matching (EATM) robot, *J. Magn. Reson.* 275 (2017) 127–136.
- [28] Z. Gan, I. Hung, X. Wang, J. Paulino, G. Wu, I.M. Litvak, P.L. Gor'kov, W.W. Brey, P. Lendi, J.L. Schiano, et al., NMR spectroscopy up to 35.2T using a series-connected hybrid magnet, *J. Magn. Reson.* 284 (2017) 125–136.
- [29] E. Kupče, R. Freeman, Adiabatic pulses for wideband inversion and broadband decoupling, *J. Magn. Reson. Ser. A* 115 (1995) 273–276.
- [30] E. Kupče, R. Freeman, Optimized adiabatic pulses for wideband spin inversion, *J. Magn. Reson. Ser. A* 118 (1996) 299–303.
- [31] L.A. O'Dell, The WURST kind of pulses in solid-state NMR, *Solid State Nucl. Magn. Reson.* 55–56 (2013) 28–41.
- [32] C. Barratt, E.D. Fackerell, D. Rosenfeld, The application of spinors to solving the Bloch equations, *J. Magn. Reson.* 85 (1989) 35–41.
- [33] R. Bhattacharyya, L. Frydman, Quadrupolar nuclear magnetic resonance spectroscopy in solids using frequency-swept echoing pulses, *J. Chem. Phys.* 127 (2007), 194503.
- [34] A. Tal, L. Frydman, Single-Scan multidimensional magnetic resonance, *Prog. Nucl. Magn. Reson. Spectrosc.* 57 (2010) 241–292.
- [35] I. Hung, Z. Gan, On the practical aspects of recording wideline QCPMG NMR spectra, *J. Magn. Reson.* 204 (2010) 256–265.
- [36] D. Kunz, Use of frequency-modulated radiofrequency pulses in MR imaging experiments, *Magn. Reson. Med.* 3 (1986) 377–384.
- [37] D. Kunz, Frequency-Modulated radiofrequency pulses in spin-echo and stimulated-echo experiments, *Magn. Reson. Med.* 4 (1987) 129–136.
- [38] V.L. Ermakov, G. Bodenhausen, Broadband excitation in magnetic resonance by self-refocusing doubly frequency-modulated pulses, *Chem. Phys. Lett.* 204 (1993) 375–380.
- [39] V.L. Ermakov, J.M. Bohlen, G. Bodenhausen, Improved schemes for refocusing with frequency-modulated chirp pulses, *J. Magn. Reson.* 2013 (1992) 226–229.
- [40] J.E. Power, M. Foroozandeh, R.W. Adams, M. Nilsson, S.R. Coombes, A.R. Phillips, G.A. Morris, Increasing the quantitative bandwidth of NMR measurements, *Chem. Commun.* 52 (2016) 2916–2919.
- [41] M. Foroozandeh, M. Nilsson, G.A. Morris, Improved ultra-broadband chirp excitation, *J. Magn. Reson.* 302 (2019) 28–33.
- [42] Z. Gan, I. Hung, Second-Order phase correction of NMR spectra acquired using linear frequency-sweeps, *Magn. Reson. Lett.* 2 (2022) 1–8.
- [43] M.S. Conradi, S.A. Altobelli, N.J. Sowko, S.H. Conradi, E. Fukushima, Adiabatic sweep pulses for Earth's ffield NMR with a surface coil, *J. Magn. Reson.* 288 (2018) 23–27.
- [44] L.B. Casabianca, D. Mohr, S. Mandal, Y.Q. Song, L. Frydman, Chirped CPMG for well-logging NMR applications, *J. Magn. Reson.* 242 (2014) 197–202.
- [45] M. Sarracanie, N. Salameh, Low-Field MRI: how low can we go? A fresh view on an old debate, *Front. Phys.* 12 (2020) 172.
- [46] B.E.G. Lucier, K.E. Johnston, W. Xu, J.C. Hanson, S.D. Senanayake, S. Yao, M. W. Bourassa, M. Srebro, J. Autschbach, R.W. Schurko, Unravelling the structure of Magnus' Pink Salt, *J. Am. Chem. Soc.* 136 (2014) 1333–1351.
- [47] D.L. Bryce, G.D. Sward, S. Adiga, Solid-State 35/37Cl NMR spectroscopy of hydrochloride salts of amino acids implicated in chloride ion transport channel selectivity: opportunities at 900 MHz, *J. Am. Chem. Soc.* 128 (2006) 2121–2134.
- [48] S.L. Veinberg, Z.W. Friedl, K.J. Harris, L.A. O'Dell, R.W. Schurko, Ultra-Wideline 14 N solid-state NMR as a method for differentiating polymorphs: glycine as a case study, *Cryst. Eng. Comm.* 17 (2015) 5225–5236.
- [49] M. Bak, J.T. Rasmussen, N.C. Nielsen, SIMPSON: a general simulation program for solid-state NMR spectroscopy, *J. Magn. Reson.* 147 (2000) 296–330.
- [50] S.K. Zaremba, Good lattice points, discrepancy, and numerical integration, *Ann. di Mat. Pura ed Appl.* 73 (1966) 293–317.
- [51] H. Conroy, Molecular Schrödinger Equation. VIII. A new method for the evaluation of multidimensional integrals, *J. Chem. Phys.* 47 (1967) 5307.
- [52] L.A. O'Dell, Direct detection of nitrogen-14 in solid-state NMR spectroscopy, *Prog. Nucl. Magn. Reson. Spectrosc.* 59 (2011) 295–318.
- [53] L.A. O'Dell, R.W. Schurko, Static Solid-State 14N NMR and computational studies of nitrogen EFG tensors in some crystalline amino acids, *Phys. Chem. Chem. Phys.* 11 (2009) 7069–7077.
- [54] S.L. Veinberg, A.W. Lindquist, M.J. Jaroszewicz, R.W. Schurko, Practical considerations for the acquisition of ultra-wideline 14N NMR spectra, *Solid State Nucl. Magn. Reson.* 84 (2017) 45–58.